Green Chemistry

PAPER

Cite this: *Green Chem.*, 2016, **18**, 2185

# Environmentally-safe and transparent superhydrophobic coatings†

J. E. Mates,‡[a] R. Ibrahim,[a] A. Vera,[a] S. Guggenheim,[b] J. Qin,[c] D. Calewarts,[c] D. E. Waldroup[d] and C. M. Megaridis*[a]

Received 13th November 2015,
Accepted 3rd December 2015

DOI: 10.1039/c5gc02725j

www.rsc.org/greenchem

The bioinspired field of superhydrophobicity has almost universally deployed environmentally-detrimental approaches relying on organic solvents and fluorinated compounds to generate liquid-repellent surfaces, thus severely limiting application at industrial scales. Recent water-borne methods have reduced the use of volatile organic compounds, but these methods often rely on either fluorinated chemistries (to lower surface energy) or charge-stabilization (to suspend roughness-enhancing particle fillers). An entirely water-based and fluorine-free superhydrophobic formulation has been developed from hydrophilic titanium dioxide ($TiO_2$) nanoparticles and polyolefin copolymers, without additional surfactants or charge-stabilization. The commercially-available ingredients are combined in a single-step, substrate-independent, wet-process application to deliver an ultra-simple, semitransparent coating which is attractive for large-area, fluid-barrier surface treatments. The coating constituents are environmentally-safe and FDA-approved, overcoming a nontrivial hurdle in the scalable development of sustainable fluid management technologies.

## Introduction

The development and implementation of water-based fluorine-free formulations for bioinspired superhydrophobic surface treatments can greatly reduce adverse environmental and biological effects typically associated with the synthesis of similar liquid-repellent coatings. Over the past several decades, many approaches to super-repellent surfaces have been developed, but synthesis often involved harsh organic solvents,[1–4] complex processing methods,[5] and/or undesirable fluorinated chemistries.[6–8] In addition, many of the demonstrated methods are not practically feasible at large scales in commercial applications;[9,10] not only for their negative environmental consequences, but also for their inability to produce large-area fluid barriers at sufficiently low cost. Imparting liquid repellency *via* a scalable spray approach has been shown viable for low-cost substrate-independent superhydrophobic coatings.[6,11–14] Following a waterborne wax-based[15] approach,[16] the use of fluorinated compounds in the present formulation has been eliminated – without need for charge stabilization. Titanium dioxide ($TiO_2$) nanoparticles are used to generate micro/nano-scale hierarchical surface roughness, and combined with a polyethylene copolymer binder to produce semitransparent superhydrophobic composite films (see Fig. 1). The present

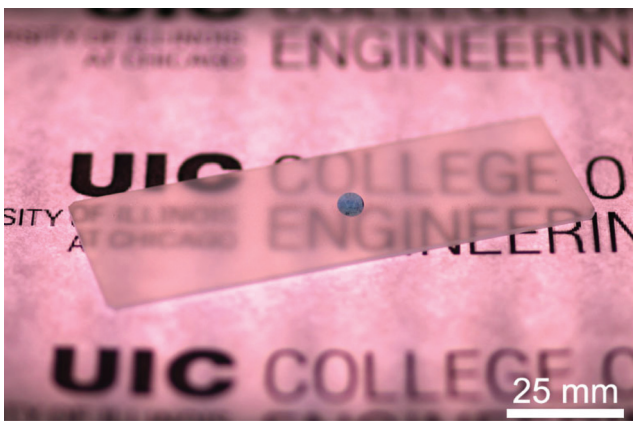


**Fig. 1** Photograph of a 10 μL water droplet (dyed blue) beaded on a coated glass slide (25 × 75 $mm^2$). The coating consists of $TiO_2$ in a polyethylene copolymer matrix, with a $TiO_2$ solid mass fraction of $\varphi = 0.75$. The tiled logo image in the background is clearly visible through the semitransparent white superhydrophobic surface treatment on the slide.

[a]*Mechanical and Industrial Engineering, University of Illinois at Chicago, Chicago, IL 60607, USA. E-mail: cmm@uic.edu*
[b]*Earth and Environmental Sciences, University of Illinois at Chicago, Chicago, IL 60607, USA*
[c]*Corporate Research and Engineering, Kimberly-Clark Corporation, Neenah, WI 54956, USA*
[d]*Corporate Research and Engineering, Kimberly-Clark Corporation, Roswell, GA 30076, USA*
†Electronic supplementary information (ESI) available. See DOI: 10.1039/c5gc02725j
‡Present address: National Research Council/Air Force Research Laboratory, Edwards AFB, CA 93524, USA.

composition does not require pH-modification and all constituent elements are FDA-approved.[17,18] The environmentally-friendly formulation is characterized below in detail, having potential in numerous fluid management applications for its simplicity, efficiency, and versatility.

The study of functional nanoparticle-polymer composites has been greatly aided by advancements in polymer synthesis, as well as greater control over nanoparticle morphologies and purities. These composites are used for a wide range of applications, such as enhanced heat transfer,[19,20] low electrical resistance,[21–23] and radiation absorption.[24,25] For liquid-repellent functionality, specifically to water (hydro-), relatively low surface energies and a suitable degree of hierarchical micro- and nano-scale roughness are required to reduce the liquid–solid interfacial contact area.[26] In combination, these two factors increase the contact angle (CA) of water droplets on the surface (CA used herein as a measure of wettability).[27] Wettability[28] by liquid on a smooth untextured surface in an air environment is determined by the free surface energies of the solid substrate constituents. Depending on whether the surface is hydrophobic or hydrophilic, interaction with water is tunable *via* surface roughness imparted with the addition of nanomaterials.[29] A high degree of surface roughness enhances the corresponding wetting behavior, either hydrophobic or hydrophilic, of the surface into two extreme cases,[30] described as either superhydrophobic or superhydrophilic (water CA greater than 150° or about 0°,[31] respectively). In general, the polymer(s) of an applied composite designates liquid affinity to the coated surface (*i.e.*, surface energy) as well as provide an adhesive matrix for embedded nanomaterials (*i.e.*, roughness).

Until recently,[32] fabrication of super-repellent polymer composites with sufficiently low surface energies ($\gamma \ll 72$ mN m$^{-1}$) required harsh solvents for wet-processing of composite elements, thus hindering the development of entirely water-based systems. Water-compatible, fluorine-free polymer systems capable of delivering low surface energy films have been the primary challenge in the development of environmentally-benign superhydrophobic coatings. In a previous formulation,[7] waterborne fluoropolymer dispersions enabled the development of aqueous superhydrophobic colloidal suspensions for coating nonwoven substrates at industrial scales. However, the fluorinated composition posed environmental concerns.[33] In 2006, the EPA initiated a reduction in the manufacture of many fluoropolymer compounds which can decompose into perfluorooctanoic acids (PFOA), having adverse environmental and biological impact. PFOA, a known cause of birth defects,[33] can pollute ground water, reservoirs, and aquatic wild-life,[34] eventually entering the human food-chain. Although short-chain fluoropolymers made in response to the EPA initiative are now available and pose less environmental risk, eliminating the necessity of fluorine altogether in extreme liquid repellency has been a primary goal of this work. The objective for future sustainable fluid barrier solutions is to make fluorinated composites obsolete by replacing them with environmentally-conscious, so-called "green" alternatives.

Particles with nanoscale dimensions allow fine control over composite surface roughness to reduce liquid–solid interfacial contact.[4] Nano-textured hydrophobic surfaces offer increased resistance to liquid wetting owing to entrained gas pockets beneath the fluid interface.[35] Many superhydrophobic surfaces utilize hydrophobic particle fillers,[6,36,37] which require non-aqueous suspensions or other additives. Although hydrophobic particle fillers aid in generating greater repellency, the charge-stabilization or surfactants required to form aqueous systems are undesirable. Hydrophilic $TiO_2$ nanoparticles produce sufficient surface roughness and are compatible with waterborne polyethylene (PE) copolymer emulsions. In a manner unique to nanoscale $TiO_2$, the polymer acts to isolate the hydrophilic nature of suspended $TiO_2$ particles in dispersion by surrounding them in a weakly hydrophobic polymer "shell" *via* surface adsorption kinetics. Hydrophobicity is maintained after composite application and drying (*i.e.*, residual water removal). Using nanoparticles of small dimensions (≤100 nm), the resultant surface roughness elevates CA into the superhydrophobic regime (>150°). $TiO_2$ is a non-toxic additive to food, skin lotions, and paint pigments[38] due to its benign environmental impact. A semitransparent, water-based, and entirely fluorine-free superhydrophobic formulation capable of large-area surface modification is currently lacking in the literature and unavailable for commercial application, but demonstrated here for the first time.

## Results and discussion

$TiO_2$ particle aggregation while in aqueous suspension varies with phase (*i.e.*, anatase or rutile), particle size, temperature and pH.[39,40] Adsorption mechanisms of anatase *vs.* rutile surfaces have been the subject of extensive study, not without some controversy. In general, smaller $TiO_2$ nanoparticles are more reactive based on the ratio of dissociative to molecular adsorption, although conflicting results have been reported.[41] Fig. 2 shows transmission electron microscope (TEM) images

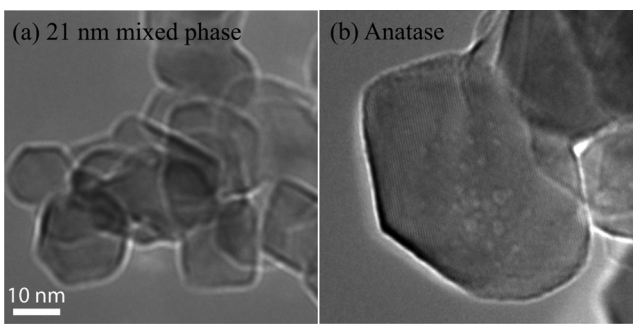


**Fig. 2** TEM images of clustered (a) 21 nm mixed-phase (anatase and rutile) $TiO_2$ primary particles, and (b) anatase $TiO_2$ particles. The 10 nm scale-bar applies to both images. The smaller primary particle size of the mixed-phase $TiO_2$ is evident and indicates a greater tendency towards aggregation over that of anatase due to its greater surface area and surface charging (*i.e.*, hydrogenation).

 

of representative samples of both anatase and 21 nm mixed-phase particles (both anatase and rutile phases are present). The latter tend to aggregate by surface charging mechanisms (*i.e.*, hydrogenation) in submicron clusters.[42] On the other hand, the all-anatase particles had a lower tendency to aggregate, as explained by their lower surface energy compared to rutile.[43] In the vacuum of the TEM column, water adsorbate is likely retained on particle surfaces, specifically the rutile component of the mixed-phase.[40] This adsorption contributes to greater aggregation owing to the presence of an adsorbate film on rutile particle surfaces. Anatase was easily identified in the TEM where primary particles were observed to be ≤60 nm in diameter; the larger anatase particle size resulted in faster settling in aqueous suspension compared to the 21 nm mixed-phase (see Fig. S1,† obtained one month after anatase and 21 nm mixed-phase suspensions were probe-sonicated in water at 5 wt% solids and allowed to settle). The 21 nm mixed-phase particles remained suspended over longer time periods without requiring additional mechanical mixing or agitation.

The ratio of filler to polymer was varied to determine an optimal formulation; composite ratios are identified in eqn (1) by the particle filler ($TiO_2$) mass fraction, $\varphi$, defined as the particle filler mass, $m_{TiO_2}$, divided by total solids mass, $m_{TiO_2+PE}$:

$$\varphi = m_{TiO_2}/m_{TiO_2+PE}. \quad (1)$$

Overall solids content was varied in terms of $\varphi$ to evaluate coating performance. Mass fractions tested were $\varphi$ = 0, 0.25, 0.5, 0.6, 0.75, and 0.8 (or, in terms of filler-to-polymer ratios, nano$TiO_2$ : PE = 0 : 100, 25 : 75, 50 : 50, 60 : 40, 75 : 25, 80 : 20, and 85 : 15). For $\varphi \leq 0.5$, inadequate roughness in the final coating achieved insufficient repellency due to the weakly hydrophobic PE blend. However, results are reported to elucidate increased water CA as a function of $\varphi$ (increased nanoroughness) in contrast to smooth untextured all-polymer ($\varphi$ = 0) coatings. The upper limit of particle filler content was fixed at $\varphi$ = 0.85, above which the polymer content was insufficient for adequate particle adhesion (*i.e.*, coating appeared "dusty"). For further details on preparation, refer to Materials and methods.

After suspending nanoparticles in water and fully dispersing *via* probe sonication, aqueous PE was added under mechanical mixing. The final dispersions were sprayed onto either aluminum foil for SEM imaging, or glass slides for CA measurements. Fig. 3 shows SEM images of dried samples (*i.e.*, anatase and two mixed-phase coatings, 21 and 100 nm, respectively) all with $\varphi$ = 0.75. Clearly, the anatase composite forms rougher texture compared to its mixed-phase variants. However, when observed under TEM (Fig. 2), anatase particles in their initial state (no PE) displayed a lower aggregation tendency. This discrepancy is likely due to surface adsorption kinetics of anatase $TiO_2$ with PE in water.[44] Anatase was

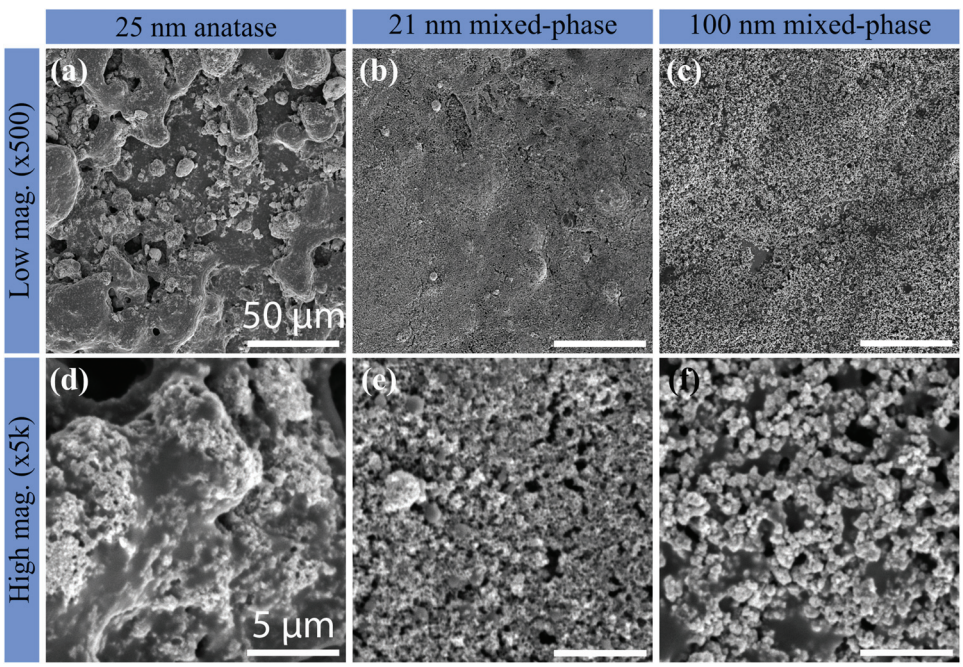


**Fig. 3** SEM images for three variant $TiO_2$ composites tested in this study (all at $\varphi$ = 0.75): (left column, a, d) anatase; (middle column, b, e) 21 nm mixed-phase (anatase + rutile); (right column, c, f) 100 nm mixed-phase. Top row (a–c) in low magnification (50 μm scale bar), and bottom row (d–f) in high magnification (5 μm scale bar). The anatase composite formed the largest particle clusters, which displayed much greater morphological inhomogeneity. The 21 nm mixed-phase composite featured uniform small aggregates, while aggregates of the 100 nm mixed-phase were slightly larger. Note the variation in visible smooth patches of exposed polymer (grey domains) in both the anatase and the 100 nm mixed-phase composites, yet the polymer appears to be evenly distributed in the 21 nm mixed-phase composite.

observed to be unstable in the PE dispersions and separated out much faster, showing the aforementioned tendency to form larger aggregates in the presence of PE but resisting aggregation in the neat powdered form. Conversely, PE acted as a stabilizing agent to prevent larger aggregates (relative to anatase) in the mixed-phase composites. Greater surface charging of the mixed-phase particles formed smaller insulated clusters upon contact with the polymer. The 21 nm mixed-phase colloidal dispersions were observed to separate slightly after one week when allowed to rest, with a thin layer of water forming near the top of the vial, but easily returning to a stable suspension once shaken. The 100 nm mixed-phase coating behaved similarly to its 21 nm mixed-phase counterpart with slightly more settling (attributed to larger particle sizes) but also returning to suspension easily upon mild mechanical mixing. Settling of the nano$TiO_2$ colloidal dispersions had negligible impact on coating performance after the dispersions were re-agitated before spraying.

Surface features of the variant composites strongly influenced water droplet mobility. The rougher texture (large aggregates) of the anatase-based coatings and distributed regions of exposed polymer are evident in the left column of Fig. 3(a and d); nanoscale $TiO_2$ aggregates (white) are seen in the bottom left high-magnification image dotting the polymer matrix (grey). Some of the large anatase-aggregate surface features approach 50 μm in size (Fig. 3a) after spray coating, while the nanoscale texture imparted by the $TiO_2$ primary particles protruding from the large structures are also seen in Fig. 3d. As mentioned prior, these nano- to micro-scale hierarchical features are critical in generating super-repellency.[45] Unfortunately, the weakly hydrophobic smooth patches of exposed polymer also detract from droplet mobility, resulting in "sticky" regions on the surface where water droplets adhere and become anchored (*i.e.*, pinning).[46] In contrast, the much smaller (submicron) aggregates in the 21 nm mixed-phase composite are highly uniform, producing consistent nanometer-scale surface roughness. Regions of smooth exposed PE are almost entirely eliminated due to a more complete adsorption of the polymer on the higher-surface-area nanoparticles. The 21 and 100 nm mixed-phase composites lacked the roughness contrast observed in the anatase samples, despite the order of magnitude difference in particle size. Although the 100 nm mixed-phase composites more closely resembled 21 nm mixed-phase coatings, the former composites had lower surface-to-volume ratios than the latter, thus preventing PE from fully covering the exposed nanoparticles. Similar to the anatase composites, regions of smooth exposed polymer were also formed in the 100 nm mixed-phase composites (grey area in Fig. 3f). In that sense, 100 nm mixed-phase composites formed a unique blend of features observed in both all-anatase and 21 nm mixed-phase composites, incorporating dual morphological and chemical aspects with a larger range of aggregate sizes and deleterious intermittent patches of smooth polymer. In all composites however, textural uniformity was evident even in the absence of chemical homogeneity (see Fig. S2†).

With the SEM results indicating that the $TiO_2$ phase is equally as important as particle size in composite formation, the kinetics of the surface interaction between titania nanoparticles and PE polymer chains were considered. As reported elsewhere,[47] $TiO_2$ particles are known to act as nucleation sites assisting in polyethylene copolymer crystallization. In general, polymers in ordered (*i.e.*, crystalline) groupings have a lower surface energy than their amorphous forms due to a more stable bonded state, and can thus contribute to greater hydrophobicity. XRD measurements were performed on variant nano$TiO_2$ composites ($\varphi$ = 0.2) compared to an all-PE ($\varphi$ = 0) composite to verify particle phase and determine polymer crystallinity enhancement. XRD measurements are inherently sensitive to volume, thus polymer content ($1 - \varphi$, assuming constant density) was fixed across all samples at 0.9 g (Fig. 4). Filler particle content was held to a minimum of 20 wt% (0.22 g, or $\varphi$ = 0.2) in the composites to better detect PE crystallinity peaks ($TiO_2$ has very pronounced crystallinity and can obscure less crystalline reflection). For the case of the all-PE sample, there are two theta peaks with values of ~19 and 22° surrounded by an amorphous "halo".[47,48] For the anatase composite, peaks from PE declined slightly in intensity coupled with a narrowing of associated peak width. Peaks from anatase were observed around 25, 38 (two peaks), 48, 54, and 55° for all samples, as expected. The mixed-phase samples had peaks indicative of rutile at 27 and 45°. However, broad reflection peaks for PE in all cases were inconclusive as to the increased crystallinity contribution from nano$TiO_2$. A slight narrowing of the peak base for anatase was accompanied by diminished peak size, resulting in an insignificant change in area under the diffraction curve. For the mixed-phase samples, peak base size remains relatively unchanged and whether or not the reflection peaks have sharpened is unclear from the background.

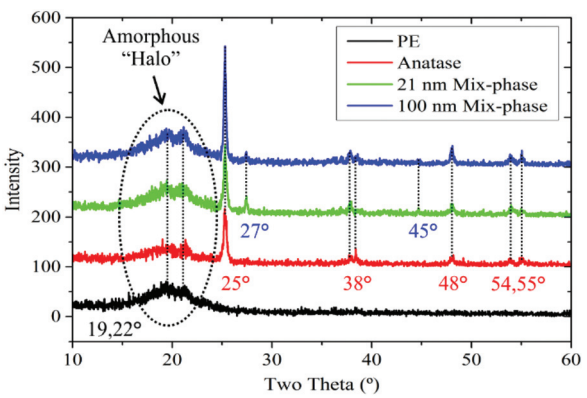


**Fig. 4** XRD patterns for an all-PE coating, or $\varphi$ = 0 (bottom, black), and three variant nano$TiO_2$ composites having mass fraction $\varphi$ = 0.2 (anatase in red, 2nd from bottom; 21 nm mixed-phase in green, 2nd from top; 100 nm mixed-phase in blue, top). Enhancement to PE crystallinity delivered by the addition of nano$TiO_2$ in any case was indeterminate due to background noise and the amorphous halo surrounding PE crystalline factions. Reflection peaks confirmed as-received anatase and mixed-phase varieties.

Additionally, PE (HYPOD™ 8510) possesses high carboxyl content from its functional pendant groups,[49] which can become dissociated upon interaction with titanium nanoparticles.[50] This reaction will generate formic acid in nano$TiO_2$ : PE dispersions, resulting in formate deposits occurring around nucleation sites (*i.e.*, grain boundaries) in the final dry composites. This was verified by comparing the pH of prepared dispersions during synthesis. PE (42 wt% in water) has an as-received alkalinity of pH ~ 9, while nano$TiO_2$ (all types) dispersed in deionized water retained neutral pH (~7). Upon combining alkaline PE polymer into the filler suspension, pH declined to about 8 in each case, suggesting a neutralizing effect brought about by reactive filler particles in the less alkaline final dispersion (pH was not affected when wet-processing $SiO_2$ or ZnO). This indicates surface adsorption mechanisms of nano$TiO_2$ likely stripped carboxylic pendant groups from the PE polymer backbone, forming desirable chemical bonds while simultaneously neutralizing the colloidal dispersion. This particle-to-polymer bonding mechanism explains the efficacy of the hydrophobic polymeric shell surrounding the otherwise hydrophilic filler particles, further strengthened when attempting comparative composites using similar oxide nanoparticle fillers, such as ZnO and $SiO_2$, both hydrophilic and with comparable dimensions. SEM images and CA results from these composites are included in the ESI as Fig. S3 and S4,† respectively. Fig. S3† illustrates that morphology and hierarchical structure for both ZnO and $SiO_2$ composites are similar to the $TiO_2$ coatings, yet CA were poor; none of the $\varphi$ values for either oxide particle achieved superhydrophobicity.

For any superhydrophobic surface, sessile apparent CA ($\theta^*$) is generally considered a first indicator for predicting dynamic droplet behavior on the surface. Variably, advancing and receding CA ($\theta_{Adv}$ and $\theta_{Rec}$, respectively) are more appropriate to characterize self-cleaning surfaces as droplet mobility is vital to the removal of surface contaminants. The magnitude of the difference in $\theta_{Adv}$ and $\theta_{Rec}$ (known as CA hysteresis $\Delta\theta = \theta_{Adv} - \theta_{Rec}$) should ideally be as close to zero as possible for best self-cleaning performance, and therefore, repellency.[27] Fig. 5 illustrates mobility of water droplets on the composite surfaces in terms of dynamic water CA ($\theta_{Adv}$ and $\theta_{Rec}$) and roll-off angle measurements, as a function of $\varphi$, for determining optimal performance. For $\varphi = 0$, $\theta_{Adv} \sim 95°$ is shown as the CA $y$-intercept for each plot; but these surfaces are "sticky," as evident by $\theta_{Rec} \sim 0°$ delivering a high $\Delta\theta$ of 95°. Water droplets experienced high adhesion to PE polymer surfaces due to its weak hydrophobicity and high CA hysteresis.

As $\varphi$ was increased, composites achieved higher CA ($\theta_{Adv}$ and $\theta_{Rec}$) and reduced CA hysteresis ($\Delta\theta \rightarrow 0°$). CA hysteresis for the mixed-phase composites diminished rapidly at increased $\varphi$, owing to the reduction of exposed polymer and higher nanoscale roughness. Exposed patches of polymer in the anatase coating allow for regions on the surface for the droplet to anchor, thus pinning the contact line and preventing droplets from receding. The hybridized regions of nano-textured and smooth polymer in the 100 nm mixed-phase composite produced variable performance as $\varphi$ increased. Performance drops off dramatically for the 100 nm composites for $\varphi >$ 0.75, resulting in more wettable surfaces due to larger nanoparticle surface area and incomplete polymer cladding. In contrast, 21 nm mixed-phase composites showed steadily improving performance with rising $\varphi$. Droplet roll-off angles are also included in Fig. 5 (grey) and verify improved repellency performance accompanying reduced $\Delta\theta$.

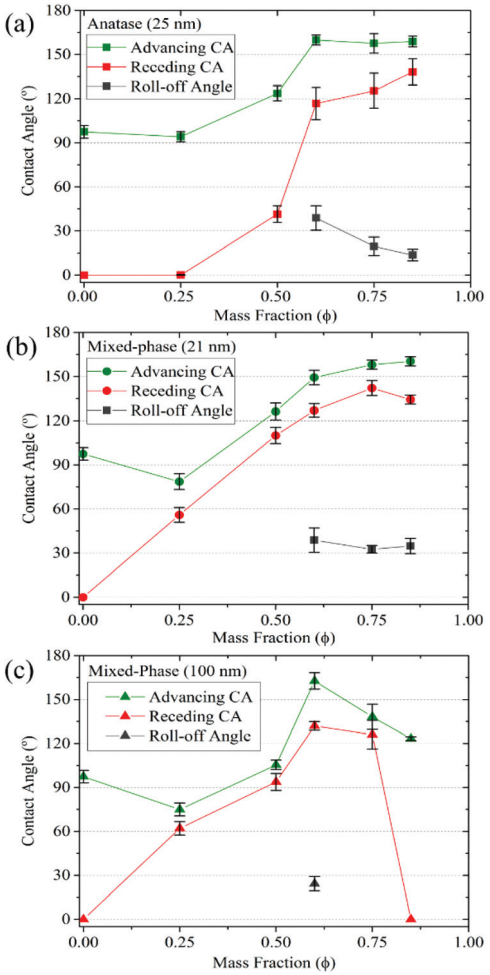


**Fig. 5** Dynamic wettability measurements for all three nano$TiO_2$-PE composite coatings tested at all mass fractions $\varphi$: (a) anatase, (b) 21 nm mixed-phase, and (c) 100 nm mixed-phase. For all samples, $\varphi >$ 0.50 boosted advancing CA (green) to above 150° (superhydrophobic) while simultaneously increasing receding CA (red). For select $\varphi$, there exists a measurable roll-off angle (grey symbols). In other cases, water droplet roll-off was not observed ("sticky" surface).

Results support that 21 nm mixed-phase $TiO_2$ particles formed optimal composites from spatially uniform morphology delivering consistent liquid repellency. Corresponding suspensions remained stable for several weeks with only minimal settling and separation, making them suitable for large-area industrial-scale surface treatments. Anatase composites are intrinsically more photo-sensitive, resulting in reduced composite repellency upon exposure to UV radiation (dissociation of

surrounding polymer) *via* increased hydrophilicity as free surface energy increases. Each variant nano$TiO_2$ was shown to be effective for achieving superhydrophobicity at $\varphi \geq 0.6$. However, reducing PE content inhibited nanoparticle adhesion above $\varphi = 0.75$. Thus, for achieving extreme repellency (high CA and sufficient droplet mobility), optimal composite blends were found between $\varphi = 0.60$ and 0.75.

## Materials and methods

### Materials

$TiO_2$ nanoparticles (titanium[IV] oxide anatase nanopowder, <25 nm particle size, 637254-100G) and two as-received mixtures of rutile and anatase (titanium[IV] oxide nanopowders, <21 nm particle size, 718467-100G; mixture of rutile and anatase, <100 nm particle size, 634662-25G) were obtained from Sigma-Aldrich to determine the effect of particle phase and size in the composite. The polyolefin (PE) blend dispersion, consisting of polyethylene-octene copolymer ~60% (adhesive elastomer) and polyethylene-acrylic acid copolymer ~40% (stabilizing agent), was obtained from DOW Chemical (~42 wt% in water; HYPOD™ 8510). Deionized water was used as a probe liquid for contact and roll-off angle measurements.

### Methods

Colloidal dispersions for spray were prepared at 5 wt% solids in water. Too low of an overall solids content required unnecessary multiple coating passes, whereas too high of a solids content increased dispersion viscosities and/or clogged the spray nozzle. A solids content of 5 wt% was found sufficient for adequate coating deposition per spray pass, and low enough to avert spray problems from high viscosities (occurring at ≥10–15 wt%). For example, to prepare 20 g of sprayable dispersion with $\varphi = 0.5$ mass fraction, 0.5 g $TiO_2$ was placed in a 20 mL vial. Subsequently, 18.3 g of deionized water was added and the mixture was probe-sonicated for 1 minute (Sonics & Materials, Inc., 750 W, 13 mm probe dia., 20% amplitude, 20 kHz). The as-received PE polymer blend was 42 wt% polymer solids in water, with the portion of water from the polymer emulsion accounted for in the final dispersion water balance. Immediately following probe-sonication of the $TiO_2$-in-water suspension, 1.19 g of PE polymer emulsion, or 0.5 g total PE solids as-received in 0.69 g water, was added to the dispersion and then mechanically mixed for 5 minutes. The water content in the final dispersions, regardless of composite ratio, was always 95 wt%.

Care was taken to ensure spray uniformity and control over coating thickness by weighing glass slide substrates before and after coating (g $m^{-2}$, or gsm). An airbrush atomizer (Paasche, VL siphon feed, 0.55 mm spray nozzle) was used to spray the prepared dispersions onto glass slides from a distance of ~20 cm. Spray distance affects composite morphology and deposition mass, and was thus selected to avoid water accumulation (longer distances) and maximize coating deposition (shorter distances). Composites formed from water-based spray dispersions can be spatially non-uniform due to slow solvent evaporation (*i.e.*, pooling). Therefore, the smallest spray nozzle was selected to enhance water evaporation during application and an electric dryer was used to evaporate residual water from the composite between spray passes, thus forming uniform films.

Characterization. Three glass slides were sprayed for each $\varphi$ tested, all of which were characterized for water CA and roll-off angles. In determining droplet mobility, water droplets were syringe-dispensed, and similarly withdrawn, using a 1 mm needle-tip, such that probe droplet diameters ranged from 1–4 mm. This facilitated dynamic measurement of advancing ($\theta_{Adv}$) and receding ($\theta_{Rec}$) CA. For roll-off angles, the glass slides were placed on a goniometer operated by a VXM motor to allow precise control through small angle increments (~0.1° $s^{-1}$) until a 10 μL water droplet was observed to roll off from its initial position. If the droplets did not roll off, the composite surfaces were deemed "sticky" and no roll-off angle is reported.

Nano$TiO_2$ particles were imaged in a transmission electron microscope (TEM; JEOL JEM-3010, 300 keV) to verify dimensions, crystalline phase morphology, and particle aggregate size. For SEM observations (Hitachi S-3000N, 5 keV), a small area (~0.25 $cm^2$) was cut from coated aluminum foil (to prevent charging) prepared in an identical manner to the glass slides. Additionally, 5 nm Pt–Pd sputter-coating was applied to the coating(s) to facilitate imaging. For X-ray diffraction (XRD) characterization (Siemens [Bruker] D5000 theta–theta powder X-ray diffractometer, 40 kV, 25 mA, Cu radiation, graphite monochromator), two theta values were varied from 10 to 60° in 0.01° increments, with 1 s per increment. Quartz background-less slides were prepared with an all-PE sample ($\varphi = 0$) compared to three variant composites (anatase, 21 nm mixture, and 100 nm mixture) in $\varphi = 0.20$ mass fraction. The all-PE slide was sprayed with 5 wt% PE in water (0.9 g PE solids). To compare PE crystallinity with the nano$TiO_2$ composites, the polymer content was fixed at 0.9 g so that the nano$TiO_2$ addition of each of the three variants was thus adjusted to 0.22 g ($\varphi = 0.2$). Low particle filler content allowed for a qualitative estimate of PE crystallinity, and was chosen to limit the strong intensity of $TiO_2$ reflection peaks.

## Conclusions

A stable, all-water-based, and fluorine-free spray dispersion has been demonstrated, achieving semitransparent superhydrophobic coatings suitable in large-area (*i.e.*, industrially scalable) fluid barrier surface treatments applicable on most common surfaces (glass, plastic, metal, *etc.*). Comprised of nano$TiO_2$ and water-borne wax polyolefin polymer, ideal ratios of formulation moieties were determined by dynamic CA measurements, emphasizing the reduction in CA hysteresis to attain droplet mobility as a critical performance metric. Optimal mass fractions were found between $\varphi = 0.6$–0.75 and achieved repeatable superhydrophobic performance, with the

 

21 nm mixed-phase (anatase + rutile) composites performing better than 25 nm anatase and 100 nm mixed-phase variants. Anatase $TiO_2$ was found to resist aggregation whereas 21 nm mixed-phase $TiO_2$ quickly formed particle groupings when each was suspended in water, most likely due to the greater presence of surface charges on rutile particles. Surface charging and high surface area explain the uniformity of spray-coated 21 nm mixed-phase film composites when combined with the alkaline polyolefin polymer blend. Moreover, such polar interactions serve to more completely sheath hydrophilic $TiO_2$ particles in the hydrophobic polymer shell. The alleged mechanism of surface adsorption cleaving carboxyl pendant groups from the PE polymer backbone was confirmed by pH measurements after the addition of the alkaline polymer, likely contributing to the effective reduction in filler particle hydrophilicity. Thus, the incorporation of a unique waterborne polymer blend is demonstrably effective for low environmental impact superhydrophobic composites, achieved *via* tuning of nanoscale roughness with variable hydrophilic titanium dioxide loading.

## Acknowledgements

Support for this work was provided by Kimberly-Clark Corp. which also contributed the polyethylene copolymer (HYPOD™ 8510) materials. J.Q., D.E.W., and C.M.M. conceived the study. J.E.M., D.C., and J.Q. conceived the material formulation. J.E.M. and C.M.M. formulated the experiments and fabrication procedures. J.E.M., R.I., and A.V. fabricated samples and performed characterization experiments. S.G. and J.E.M. performed XRD analysis. J.E.M. and C.M.M. analyzed the data and wrote the manuscript with input from all authors. The authors thank Mohamed Elsharkawy for assistance with TEM imaging.

## Notes and references

1 P. N. Manoudis, I. Karapanagiotis, A. Tsakalof, I. Zuburtikudis and C. Panayiotou, *Langmuir*, 2008, **24**, 11225–11232.
2 Y. K. Kang, J. Y. Wang, G. B. Yang, X. J. Xiong, X. H. Chen, L. G. Yu and P. Y. Zhang, *Appl. Surf. Sci.*, 2011, **258**, 1008–1013.
3 C.-F. Wang and S.-J. Lin, *ACS Appl. Mater. Interfaces*, 2013, **5**, 8861–8864.
4 X. Tang, T. Wang, F. Yu, X. Zhang, Q. Zhu, L. Pang, G. Zhang and M. Pei, *RSC Adv.*, 2013, **3**, 25670–25673.
5 S. G. Lee, D. Y. Lee, H. S. Lim, D. H. Lee, S. Lee and K. Cho, *Adv. Mater.*, 2010, **22**, 5013–5017.
6 L. Gao and J. He, *J. Colloid Interface Sci.*, 2013, **396**, 152–159.
7 J. E. Mates, T. M. Schutzius, I. S. Bayer, J. Qin, D. E. Waldroup and C. M. Megaridis, *Ind. Eng. Chem. Res.*, 2014, **53**, 222–227.
8 K. Chen, S. Zhou and L. Wu, *Chem. Commun.*, 2014, **50**, 11891–11894.
9 A. Nakajima, A. Fujishima, K. Hashimoto and T. Watanabe, *Adv. Mater.*, 1999, **11**, 1365–1368.
10 S. Y. Xing, J. Jiang and T. R. Pan, *Lab Chip*, 2013, **13**, 1937–1947.
11 I. S. Bayer, M. K. Tiwari and C. M. Megaridis, *Appl. Phys. Lett.*, 2008, **93**, 3.
12 W. C. Wu, X. L. Wang, X. J. Liu and F. Zhou, *ACS Appl. Mater. Interfaces*, 2009, **1**, 1656–1661.
13 J. E. Mates, T. M. Schutzius, J. Qin, D. E. Waldroup and C. M. Megaridis, *ACS Appl. Mater. Interfaces*, 2014, **6**, 12837–12843.
14 T. M. Schutzius, I. S. Bayer, G. M. Jursich, A. Das and C. M. Megaridis, *Nanoscale*, 2012, **4**, 5378–5385.
15 F. J. Lang, P. H. Clough, T. J. Dyer, M. T. Goulet, K.-C. Liu, M. R. Lostocco, D. J. Nickel, M. J. Rekoske, T. M. Runge, M. L. Seabaugh, J. J. Timm and K. J. Zwick, *U.S. Patent*, 7588662B2, 2009.
16 T. M. Schutzius, I. S. Bayer, J. Qin, D. Waldroup and C. M. Megaridis, *ACS Appl. Mater. Interfaces*, 2013, **5**, 13419–13425.
17 Food and Drug Administration, *Code of Federal Regulations (Dept. of Health and Human Services)*, 2014, vol. 1, p. 73.
18 The Dow Chemical Co., *Inventory of Effective Food Contact Substance Notifications*, 2004, FCN No. 424.
19 X. Chen, J. Wu, R. Ma, M. Hua, N. Koratkar, S. Yao and Z. Wang, *Adv. Funct. Mater.*, 2011, **21**, 4617–4623.
20 N. Miljkovic, R. Enright and E. N. Wang, *ACS Nano*, 2012, **6**, 1776–1785.
21 M. Li, J. Zhai, H. Liu, Y. L. Song, L. Jiang and D. B. Zhu, *J. Phys. Chem. B*, 2003, **107**, 9954–9957.
22 J. T. Han, S. Y. Kim, J. S. Woo and G.-W. Lee, *Adv. Mater.*, 2008, **20**, 3724–3727.
23 J. E. Mates, I. S. Bayer, M. Salerno, P. J. Carroll, Z. Jiang, L. Liu and C. M. Megaridis, *Carbon*, 2015, **87**, 163–174.
24 A. Das, H. T. Hayvaci, M. K. Tiwari, I. S. Bayer, D. Erricolo and C. M. Megaridis, *J. Colloid Interface Sci.*, 2011, **353**, 311–315.
25 Y. J. Chen, Y. Li, M. C. Yip and N. Tai, *Compos. Sci. Technol.*, 2013, **80**, 80–86.
26 A. Lafuma and D. Quere, *Nat. Mater.*, 2003, **2**, 457–460.
27 J. F. Joanny and P. G. Degennes, *J. Chem. Phys.*, 1984, **81**, 552–562.
28 R. N. Wenzel, *Ind. Eng. Chem.*, 1936, **28**, 988–994.
29 A. B. D. Cassie and S. Baxter, *Trans. Faraday Soc.*, 1944, **40**, 546–551.
30 K. Tadanaga, J. Morinaga, A. Matsuda and T. Minami, *Chem. Mater.*, 2000, **12**, 590–592.
31 R. Wang, K. Hashimoto, A. Fujishima, M. Chikuni, E. Kojima, A. Kitamura, M. Shimohigoshi and T. Watanabe, *Nature*, 1997, **388**, 431–432.
32 C. M. Megaridis, T. M. Schutzius, I. S. Bayer and J. Qin, *U.S. Patent*, 20130030098A1, 2013.
33 C. Lau, J. L. Butenhoff and J. M. Rogers, *Toxicol. Appl. Pharmacol.*, 2004, **198**, 231–241.

34 J. W. Martin, S. A. Mabury, K. R. Solomon and D. C. G. Muir, *Environ. Toxicol. Chem.*, 2003, **22**, 189–195.
35 D. Quere, *Rep. Prog. Phys.*, 2005, **68**, 2495–2532.
36 M. K. Tiwari, I. S. Bayer, G. M. Jursich, T. M. Schutzius and C. M. Megaridis, *ACS Appl. Mater. Interfaces*, 2010, **2**, 1114–1119.
37 H. Ogihara, J. Xie, J. Okagaki and T. Saji, *Langmuir*, 2012, **28**, 4605–4608.
38 A. Weir, P. Westerhoff, L. Fabricius, K. Hristovski and N. von Goetz, *Environ. Sci. Technol.*, 2012, **46**, 2242–2250.
39 J. M. Pettibone, D. M. Cwiertny, M. Scherer and V. H. Grassian, *Langmuir*, 2008, **24**, 6659–6667.
40 S. Salameh, J. Schneider, J. Laube, A. Alessandrini, P. Facci, J. W. Seo, L. C. Ciacchi and L. Maedler, *Langmuir*, 2012, **28**, 11457–11464.
41 J. J. Liang, Y. Wang, Y. Huang, Y. F. Ma, Z. F. Liu, F. M. Cai, C. D. Zhang, H. J. Gao and Y. S. Chen, *Carbon*, 2009, **47**, 922–925.
42 A. S. Barnard and L. A. Curtiss, *Nano Lett.*, 2005, **5**, 1261–1266.
43 A. S. Barnard, P. Zapol and L. A. Curtiss, *J. Chem. Theory Comput.*, 2005, **1**, 107–116.
44 M. A. Henderson, *Surf. Sci. Rep.*, 2002, **46**, 1–308.
45 C. X. Wang, T. J. Yao, J. Wu, C. Ma, Z. X. Fan, Z. Y. Wang, Y. R. Cheng, Q. Lin and B. Yang, *ACS Appl. Mater. Interfaces*, 2009, **1**, 2613–2617.
46 J. Xi and L. Jiang, *Ind. Eng. Chem. Res.*, 2008, **47**, 6354–6357.
47 D. M. Panaitescu, C. Radovici, M. Ghiurea, H. Paven and M. D. Iorga, *Polym.-Plast. Technol. Eng.*, 2011, **50**, 196–202.
48 B. Jongsomjit, S. Ngamposri and P. Praserthdam, *Catal. Lett.*, 2005, **100**, 139–146.
49 R. Wevers and J. Vyorykka, Presented at 12th TAPPI European PLACE Conference, Budapest, Hungary, 2009.
50 U. Diebold, *Surf. Sci. Rep.*, 2003, **48**, 53–229.

 